Available online at www.sciencedirect.com
SCIENCE DIRECT®
Computers and Mathematics with Applications 52 (2006) 749–758
An International Journal
computers & mathematics with applications
www.elsevier.com/locate/camwa

Sperm Motility and Multiciliary Beating: An Integrative Mechanical Model

R. H. DILLON
Department of Mathematics
Washington State University
Pullman, WA 99163, U.S.A.

L. J. FAUCI
Department of Mathematics
Tulane University
New Orleans, LA 70118, U.S.A.

XINGZHOU YANG
Center for Computational Science
Tulane University
New Orleans, LA 70118, U.S.A.

Abstract—The motility of sperm flagella and cilia are based on a common axonemal structure. In this article, we describe a fluid-mechanical model for the ciliary and sperm axoneme. This fluid-mechanical model, based on the immersed boundary method, couples the internal force generation of dynein molecular motors through the passive elastic axonemal structure with the external fluid mechanics governed by the Navier-Stokes equations. We show recent numerical simulation results for sperm motility and multiciliary interaction.

1. INTRODUCTION

The mathematical modeling of sperm motility and ciliary motion has a rich history with the pioneering work of Taylor [1], Gray and Hancock [2] and Lighthill [3] as well as more recent contributions by many others (for review, see [4]). Nevertheless, there remain several open scientific questions in ciliary and sperm mechanics: what mechanisms govern the activation of dyneins to produce the wide variety of flagellar and ciliary waveforms? What are the mechanisms governing multiciliary wave forms? What is the mechanical basis for hyperactivation in sperm and what is the steering mechanism for sperm in those species that are chemotactic?

The typical "9 + 2" axoneme, as shown in Figure 1, consists of a central pair of singlet microtubules surrounded by nine outer doublet microtubules and encased by the cell membrane (cf. [5,6] for review). The nine outer doublets are connected by radial spokes to a sheath surrounding the central pair. In addition, the outer doublets are connected by protein structures, named nexin links, between adjacent pairs of doublets. Two rows of dynein arms extend from an outer doublet toward an adjacent doublet at regularly spaced intervals. The bending of the

This research has been supported by an NSF Grant DMS-0201063. The computations of all the simulations were obtained on SGI and AMD clusters at Center of Computational Science, Tulane University, and some were recomputed on Alpha computers at Department of Mathematics, Washington State University.

0898-1221/06/$ - see front matter Typeset by AMS-TEX
doi:10.1016/j.camwa.2006.10.012

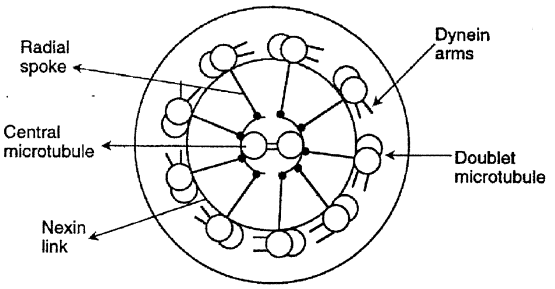

Figure 1. Diagram of the "9 + 2" axoneme.

axoneme is caused by sliding between pairs of outer doublets. Active sliding is due to the unidirectional ATP-induced force generation of the dynein power stroke. Backward, passive sliding is due to the active sliding of other pairs of doublets within the axoneme. The precise nature of the spatial and temporal control mechanisms regulating the various flagellar and ciliary beats is still unknown.

In [7], a model of an idealized cilium was introduced. This model, based on the immersed boundary method [8], incorporated a mechanical representation of the cilium's axoneme and discrete representations of the individual dynein motors coupled to the fluid mechanics governed by the Navier-Stokes equations. A model for sperm motility was introduced in [9]. The sperm model utilized the axonemal structure of the cilium model coupled with a simple curvature controlled dynein activation mechanism. In this article, we give a description of the cilia and sperm models and show recent simulation results for sperm motility based on a curvature threshold mechanism, as well as simulations of multiciliary interactions.

2. MATHEMATICAL MODEL

The formulation of our model is based on the immersed boundary method, first introduced by Peskin [8] to model blood flow in the heart. This method provides a framework for coupling the elastic dynamics of cilia and sperm flagella with a viscous incompressible fluid (for recent reviews, see [10,11]). This method treats neutrally-buoyant elastic boundaries immersed in a fluid as regions of fluid in which additional forces are applied. These elastic boundaries may be thought of as delta-function layers of force that exert force on the fluid and alter its motion, but at the same time move at the local fluid velocity. The immersed boundary method has been used in a variety of biological applications including the study of sperm motility in the reproductive tract [12], platelet aggregation [13], biofilm processes [14,15], three-dimensional blood flow in the heart [16,17], arteriolar flow [18], limb development [19], and large deformation of red blood cells [20].

The structure of the two-dimensional model axoneme consists of microtubules (see Figure 2a). Each of the axoneme's two microtubules consists of two filaments with diagonal cross-links. The filaments are highly resistant to stretching and compression but offer no resistance to bending. Resistance to bending of the microtubules is governed by the elastic properties of the diagonal cross-links. Adjacent pairs of microtubules are interconnected with horizontal links representing the nexin links of the axoneme. Dynein motors are represented as dynamic diagonal elastic links between adjacent pairs of microtubules. These elastic springs may form, change connectivity, and be broken during the course of the computations. Dynamic link formulations have been used in other immersed boundary calculations to model cell-cell cohesion in platelet aggregation [13] and biofilm formation [14]. In addition, dynamic links have been used to simulate a viscoelastic fluid within the immersed boundary framework in [21].

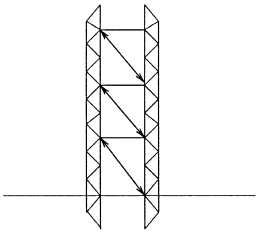

(a) Schematic of cilia axoneme in (LR) mode.

(b) Sperm.

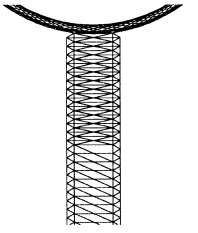

(c) Detail of sperm axoneme, basal body and head.

Figure 2.

In cilia and flagella, the active sliding between adjacent pairs of microtubules can occur in only one direction. Thus, dyneins on different pairs of microtubules must be activated in order to produce a ciliary or flagellar beat. We accomplish this in our model by allowing two configurations. In the *left to right* configuration shown in the schematic, designated *LR mode*, the dyneins are permanently attached to fixed nodes on the left microtubule. Dynein attachment on the opposite microtubule attachment sites can be transitory. Contraction of the dynein generates sliding between the two microtubules with the right-hand microtubule moving upwards relative to the left. Since the pair of microtubules is tethered at the base, sliding is converted to bending and the tip moves toward the right. In the *right to left* configuration, designated *RL mode* (not shown), the dyneins are permanently attached to fixed nodes on the right-hand microtubule and extend downward toward transitory attachment sites on the left-hand microtubule. As the dyneins contract, the left-hand microtubule moves upward relative to the right-hand microtubule and the tip moves toward the left. In either configuration, one end of a dynein can attach, detach, and reattach to attachment sites on the microtubule. In our model of flagellar swimming, some of the dyneins are in *LR mode* and others in *RL mode*.

A structure representing the cell body may be included as shown in Figure 2b. The model for the sperm axoneme includes a specialized basal region adjacent to the cell body as shown in Figure 2c. The model basal body includes a network of elastic elements extending from one microtubule to the other which are designed to restrict relative movement between the two microtubules. Dyneins and nexin links are deleted from this basal region. Although cilia also have basal bodies in the region near the cell wall, this has not yet been included in the cilia models.

2.1. Mathematical Framework

The fluid is regarded as viscous and incompressible, and the microtubule filaments that compose the sperm or cilium are elastic boundaries immersed in this fluid. The other structures within the axoneme are represented as forces which act upon the filaments. We assume that the flow is governed by the Navier-Stokes equations

$$\rho\left[\frac{\partial \mathbf{u}}{\partial t} + \mathbf{u}\cdot\nabla\mathbf{u}\right] = -\nabla p + \mu\Delta\mathbf{u} + \mathbf{F}(\mathbf{x},t), \tag{1}$$

$$\nabla\cdot\mathbf{u} = 0, \tag{2}$$

which describe the balance of momentum and conservation of mass in a viscous incompressible fluid. Here ρ is the fluid density, μ is the fluid viscosity, $\mathbf{u} = (u, v)$ is the fluid velocity, p denotes the pressure, and $\mathbf{F}$ is the force density (force per unit area in two dimensions) which is exerted on the fluid by the axoneme and cell membrane.

The force density $\mathbf{F}$ in equation (1)

$$\mathbf{F} = \mathbf{F}_M + \mathbf{F}_N + \mathbf{F}_D + \mathbf{F}_C \tag{3}$$

includes contributions arising from the deformation of the elastic structure of the microtubules $\mathbf{F}_M$, elongation of the nexin links $\mathbf{F}_N$, contraction of the dynein links $\mathbf{F}_D$ as well as forces on the cell membrane that maintain the shape of the cell body $\mathbf{F}_C$.

Each of the microtubules, in this two-dimensional model, is represented at time t as a pair of one-dimensional filaments, $\mathbf{X}^k(s,t)$, indexed by a Lagrangian parameters s (arclength in an unstressed configuration). The force per unit length $\mathbf{f}^k(s,t)$

$$\mathbf{f}^k = \mathbf{f}^k_M + \mathbf{f}^k_N + \mathbf{f}^k_D + \mathbf{f}^k_C \tag{4}$$

along the k^{th} filament includes contributions from elastic structure of the microtubules $\mathbf{f}^k_M$, nexin links, $\mathbf{f}^k_N$, dynein links $\mathbf{f}^k_D$, and cell-wall forces $\mathbf{f}^k_C$. The force densities $\mathbf{F}_X$, $X = M, N, D, C$, in equation (3) are obtained via integration

$$\mathbf{F}_X(\mathbf{x},t) = \sum_k \int \mathbf{f}^k_X(s,t)\delta\left(\mathbf{x} - \mathbf{X}^k(s,t)\right)\, ds. \tag{5}$$

Here, the integrations are over the filaments, and δ is the two-dimensional Dirac delta function. This integral communicates the force defined on the immersed boundaries (filaments) to a force defined in all of space. Of course, the force $\mathbf{F}_X$ is nonzero only at points in space that coincide with immersed boundary points.

Our coupled fluid-axoneme system is closed by requiring that the velocity of the microtubules and cell membrane must be equal to the local fluid velocity at each point.

$$\frac{\partial \mathbf{X}^K(s,t)}{\partial t} = \mathbf{u}\left(\mathbf{X}^k(s,t),t\right) = \int \mathbf{u}(\mathbf{x},t)\delta\left(\mathbf{x} - \mathbf{X}^k(s,t)\right)\, d\mathbf{x}. \tag{6}$$

Here the integration is over the entire fluid domain.

In the following we describe the discretized version of the model system. The microtubule filaments $\mathbf{X}^k(s,t)$ are discretized and represented as *immersed boundary points* or *nodes* $\mathbf{X}^k_i(t)$ with $i = 1, \ldots, N_p$. Similarly, the microtubule forces $\mathbf{f}^k_X(s,t)$ are represented as discrete forces $\mathbf{f}^k_{X,i}(t)$ at the immersed boundary points.

2.2. Microtubules and Cell Membrane

We represent each microtubule as a pair of filaments with additional cross-link forces between the filaments. The filaments themselves are composed of individual elastic links. The diagonal cross-links and filament links attach at the immersed boundary points. In the configuration shown in Figure 2a, pairs of upper and lower cross-links form equilateral triangles with the associated filament links. The N_p nodes on each filament are indexed with $i = 1, \ldots N_p$ from base to tip[1] and we imagine that between each pair of successive points $\mathbf{X}^k_i$, $\mathbf{X}^k_{i+1}$ on a microtubule filament, there is an elastic spring or 'link' which generates forces to push the link's length toward a specified resting length. As illustrated in Figure 2, each immersed boundary point is connected by elastic springs to the two nearest nodes on the same filament as well as to the two nearest nodes on the opposite filament of the same microtubule via diagonal elastic springs. The microtubule forces $\mathbf{f}^k_{M,i}(t)$ include a contribution from the link between the i^{th} node and the $(i+1)^{\text{th}}$ node on the same filament of the form

$$-S_f\left(\left\|\mathbf{X}^k_{i+1} - \mathbf{X}^k_i\right\| - \Delta s_f\right)\frac{\mathbf{X}^k_i - \mathbf{X}^k_{i+1}}{\left\|\mathbf{X}^k_i - \mathbf{X}^k_{i+1}\right\|}. \tag{7}$$

This force is, therefore, a stiffness constant (S_f) times the deviation from rest length (Δs_f) and is applied tangent to the spring. In addition forces due to the elastic diagonal cross-links are

[1]As shown in the schematic (Figure 2), each of the inner filaments has two more nodes than the outer filaments. As a result, the outer filaments of the axoneme are indexed with $i = 2, \ldots N_p - 1$.

also generated. The equations for the diagonal forces are similar to equation (7) with stiffness constant S_d and resting length $\Delta s_d = \Delta s_f$. The sum of the forces at the i^{th} node on the k^{th} filament due to the elastic links along the filament and diagonal cross-links is given by $\mathbf{f}^k_{M,i}(t)$.

The cell membrane is modeled by including additional elastic forces of the form shown in equation (7). The configuration of the cell membrane links for sperm is illustrated in Figure 2c. For cilia, the immersed boundary points of the cell membrane are tethered to fixed points in space by means of stiff elastic links.

2.3. Dyneins and Nexin Links

Dyneins are represented in the model as elastic links between the two microtubules. The dynein forces are applied at the immersed boundary points on the inner filaments ($k = 2$ and $k = 3$) as shown in Figure 2. During the course of a simulation, two families of dyneins are tracked:

- LR mode. These dyneins are oriented diagonally downwards from the left microtubule to the right microtubule. If activated, these dyneins contract and the right microtubule slides distally relative to the left microtubule.
- RL mode. These dyneins are oriented diagonally downwards from the right microtubule to the left microtubule. If activated, these dyneins contract and the left microtubule slides distally relative to the right microtubule.

The model schematic shown in Figure 2a illustrates the dynein configuration for the LR mode along the entire length of the axoneme. Dynein elastic links are shown connecting the i^{th} node on the inner filament of the left microtubule with the $(\bar{i} - M)^{\text{th}}$ node on the right microtubule. The index $\bar{i}$ is the closest node on the inner filament of the right microtubule. The offset M is set at 2 for all of the simulations shown in this paper. Let $\mathbf{X}^L_i$ for $i = 1, \ldots, N_p$ be the immersed boundary points along the inner filament of the left microtubule and $\mathbf{X}^R_i$ be the nodes along the inner filament of the right microtubule. Similarly, let $\mathbf{f}^L_i$ and $\mathbf{f}^R_i$ be the dynein forces at these immersed boundary points. The equation for the dynein force at $\mathbf{X}^L_i$ in the LR mode is

$$\mathbf{f}^L_i = -S_{\text{dyn}} \left(\mathbf{X}^L_i - \mathbf{X}^R_{\bar{i}-M} \right), \tag{8}$$

where S_{dyn} is the dynein spring force parameter. The dynein forces at each end of the dynein are equal and opposite with $\mathbf{f}^R_{\bar{i}-M} = -\mathbf{f}^L_i$. Dynein forces in the RL mode are described similarly. Note the dynein force is represented as a linear elastic spring with zero resting length. This discussion applies to dyneins that are currently active. The activation of dyneins will discussed below.

Dynein connectivity is reassessed at each time step of a numerical simulation. As the microtubules slide, the endpoint of a dynein link may 'ratchet' from one node of the microtubule to another. Nexin links are also represented in this model. In the LR mode as shown in Figure 2, the nexins form a link between the inner filaments connecting the node at $\mathbf{X}^R_i(t)$ with $\bar{\mathbf{X}}^L_i$ where $\bar{\mathbf{X}}^L_i$ is the closest *point* on the left, inner filament. The equation for the nexin link force $\mathbf{f}^R_{N,i}$ at the node $\mathbf{X}^R_i$ is

$$\mathbf{f}^R_{N,i}(t) = -S_N \left(\left\| \mathbf{X}^R_i - \bar{\mathbf{X}}^L_i \right\| - \Delta s_N \right) \frac{\bar{\mathbf{X}}^L_i - \mathbf{X}^R_i}{\left\| \bar{\mathbf{X}}^L_i - \mathbf{X}^R_i \right\|}. \tag{9}$$

The force at $\bar{\mathbf{X}}^L_i$ is $-\mathbf{f}^R_{N,i}$. Thus the nexin link force is a normal force applied orthogonally to the tangent lines of the filaments at the two points. The force applied has force constant S_N and resting length Δs_N. The latter is chosen to be the resting length separating distance between the two microtubules.

The dynein force parameter S_{dyn} in equation (8) at the i^{th} dynein may depend upon the local intermicrotubule spacing z_i. In LR mode $z_i = \|\mathbf{X}^R_i - \bar{\mathbf{X}}^L_i\|$ with a similar expression in the RL model. We assume that the dynein spring parameter has the form $S_{\text{dyn}}(z) = \hat{S}_{\text{dyn}} g(z)$. The form of g is described in [9].

The dynein forces and nexin forces described here can also be viewed as a single mechanism describing a model dynein. The tangential forces of the diagonal links generate the shear forces and are responsible for sliding, whereas the nexin forces resist changes in intermicrotubule spacing.

2.4. Force Field

The forces due to all of the springs representing the filament links, diagonal cross-links, nexin links, and dyneins contribute to the force density function at each of the nodes. A discrete version of equation (3) is used to spread this force density defined along microtubules to a force field on the fluid domain. The microtubule point forces are distributed to the fluid by the use of an approximate delta function of the form $\delta_h(\mathbf{x}) = d(x)d(y)$ where h is mesh width of the finite difference fluid grid and

$$d(r) = \begin{cases} \dfrac{1}{4h}\left(1 + \cos\dfrac{\pi r}{2h}\right), & |r| < 2h, \\ 0, & |r| \geq 2h. \end{cases} \tag{10}$$

We refer the reader to [8] for details.

The discrete version of the microtubule force field $\mathbf{F}_M$ is given by

$$\mathbf{F}_M(\mathbf{x}, t) = \sum_{i,k} \mathbf{f}^k_{M,i}(t)\delta_h\left(\mathbf{x} - \mathbf{X}^k_i(t)\right)\Delta s_f. \tag{11}$$

The cell wall force field is obtained similarly.

The active dynein force field $\mathbf{F}_D$ is given by

$$\mathbf{F}_D(\mathbf{x}, t) = \sum_i \left(\mathbf{f}^L_i(t)\delta_h\left(\mathbf{x} - \mathbf{X}^L_i(t)\right) + \mathbf{f}^R_i(t)\delta_h\left(\mathbf{x} - \mathbf{X}^R_i(t)\right)\right)\Delta s_f. \tag{12}$$

Similar equations are used to obtain the nexin link force field.

2.5. Numerical Algorithm

We can summarize the immersed boundary algorithm as follows: suppose that at the end of timestep n we have the fluid velocity field $\mathbf{u}^n$ on a grid, and the configuration of the immersed boundary points comprising the filaments of the microtubules $(\mathbf{X}^k)^n$ and the cell membrane $(\mathbf{X}_c)^n$. Then to advance the system by one timestep we:

1. Reassess the connectivity structure of dynein motors and nexin links.
2. Decide upon the activation of dyneins based upon the configuration of the filaments of the microtubules $(\mathbf{X^k})^\mathbf{n}$.
3. Calculate the force densities $\mathbf{f^k}$ from the microtubule boundary configuration, dyneins and nexin links.
4. Calculate the force densities $\mathbf{f}_c$ from the cell membrane configuration $(\mathbf{X}_c)^n$.
5. Spread the force densities to the grid to determine the forces $\mathbf{F}$ on the fluid.
6. Solve the Navier-Stokes equations for the fluid velocities $\mathbf{u}^{n+1}$.
7. Interpolate the fluid velocity field to each immersed boundary point $(\mathbf{X}^k)^n$ and $(\mathbf{X}_c)^n$ and move the point at this local fluid velocity.

It is in Steps (1) and (2) that we implement different dynein activation strategies. The kinetics of individual dynein activation may depend upon the geometry of the structure, such as local curvature, shear and intermicrotubule spacing. In addition, the activation kinetics may be stochastic. For a comprehensive discussion of the modeling of dynein activation, see [5].

The crucial feature of this fluid-structure interaction model is that the axoneme is not the computational boundary in the Navier-Stokes solver. This immersed boundary is the source of a dynamic force field which influences the fluid motion through the force term in the fluid equations. This allows us to easily simulate the interaction of several cilia or sperm efficiently.

Since the computational domain is a fixed rectangle, we can use an efficient fluid solver designed for a regular grid with simple boundary conditions. For Step (6) we use a finite difference scheme with periodic boundary conditions. This method, described in detail in [19], is a fast Fourier transform method suited for low Reynolds numbers. Steps (5) and (7) involve the use of the discrete delta function shown in equation (10) which communicates information between the grid and the immersed boundary points.

3. NUMERICAL RESULTS: SPERM FLAGELLAR MOTION

In [9] we presented a dynein activation mechanism for sperm flagellar motion which we shall refer to as the LAG model. In the LAG model, dyneins in a given location at time t were set in the LR (RL) mode if the curvature at that site were positive (negative) at time $t-\tau$, where $\tau > 0$. Thus present dynein activation would depend on the sign of curvature at time τ in the past. The LAG parameter τ was typically in the range of several milliseconds and could be regarded as the composite time lag of the various physical and chemical stages in the dynein activation cycle.

In the THRESHOLD model presented here, a dynein mode switches from RL to LR if the local curvature exceeds a specified positive threshold value TH. Similarly, the dynein switches from LR to RL mode when the local curvature falls below a specified negative threshold value $-$ TH. Once the mode is switched, the activation of the dynein is delayed by a time τ. This is similar to the LAG model wherein TH $= 0$.

In Figure 3 we show simulation results of the sperm model using the THRESHOLD model for dynein activation. In this simulation the fluid viscosity is that of water (1 cp). The flagella exhibits a beat frequency of approximately 78 Hz. The four frames shown here illustrate the flagellar waveform over 1.5 beats. In Figure 4 we show snapshots at time $t = 0.06$ s from three different simulations with viscosities of 1 cp, 5 cp, and 10 cp. We see a reduction of swimming speed, flagellar amplitude and wavelength as fluid viscosity is increased. In the LAG model we observed a reduction of swimming speed, but increased flagellar amplitude and no change in flagellar wavelength as fluid viscosity increased [9]. Thus the LAG and THRESHOLD models exhibit significant differences in the response to changes in fluid viscosity. The LAG and THRESHOLD models are based on dynein activation schemes originally proposed by [22–25]. See also [26,27].

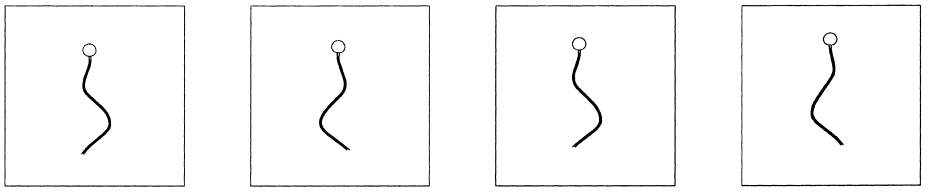

(a) 0.0120 s. (b) 0.0184 s. (c) 0.248 s. (d) 0.0312 s.

Figure 3. Snapshots of sperm swimming with THRESHOLD dynein activation at times.

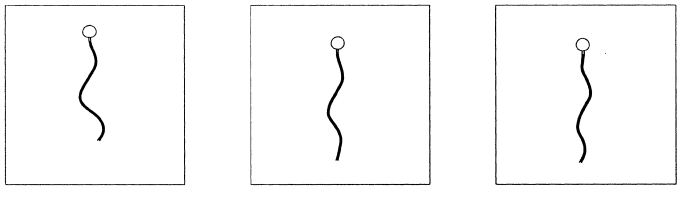

(a) 1 cp. (b) 5 cp. (c) 10 cp.

Figure 4. THRESHOLD model with changes in viscosity.

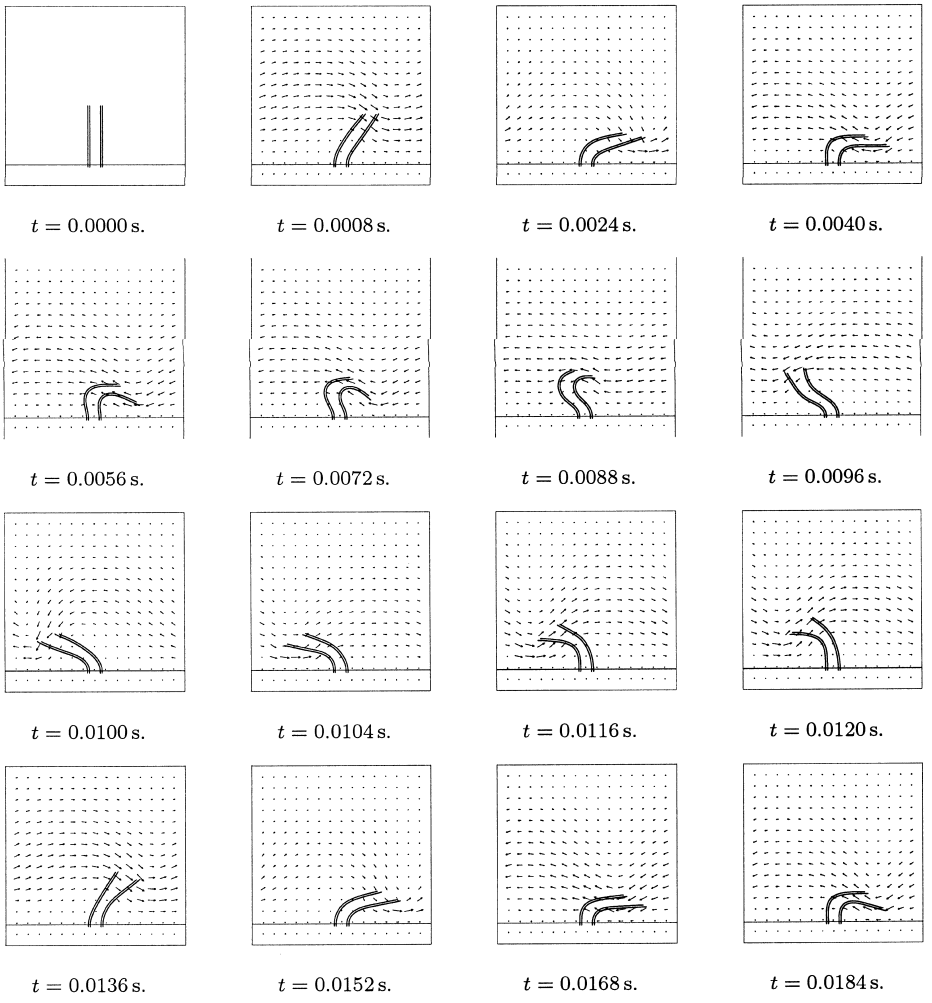

Figure 5. Snapshots of cilia with velocity fields at selected times.

4. NUMERICAL RESULTS: MULTICILIARY MOTION

The multicilia model is an extension of the single cilium model described above. The axoneme of each cilia in the model system is based on the structure shown in Figure 2a. Here we show the results of numerical simulations for a two-ciliary model. In each of these simulations, our fluid domain is $40\,\mu\text{m} \times 40\,\mu\text{m}$. The finite difference grid we used is 256×256. In the configuration of cilia, the length of each cilium is approximately $14\,\mu\text{m}$. The spacing between cilia in each simulation is $2.8125\,\mu\text{m}$. We employ a geometric switch as described in [7] to determine when the cilium beat changes directions. That is, the ciliary beat changes its directions once the shear between microtubules has exceeded a specified threshold. In the simulations shown here, the switch occurs when the dynein attachment site at the tip is eight attachment sites from its initial configuration. The beat of each cilium changes its direction independently. In recovery stroke, the dynein activation wave front is controlled by the curvature control algorithm used in [7].

In Figure 5, we show snapshots of velocity fields at different times. In this simulation, the two cilia are parallel at $t = 0\,\text{s}$. At $t = 0.0008\,\text{s}$ and $t = 0.0024\,\text{s}$, the ciliary beat is in its power stroke, but at $t = 0.004\,\text{s}$, the ciliary beat is in the recovery stroke (note the direction of the velocity fields). The beating frequency in Figure 5 is about 59 Hz. We show in Figures 6 and 7 results from a single simulation. At the beginning of the simulation, as shown in Figure 6, the beats of the two cilia are out of phase. By time $t = 0.0560\,\text{s}$, as shown in Figure 7, the cilia exhibit

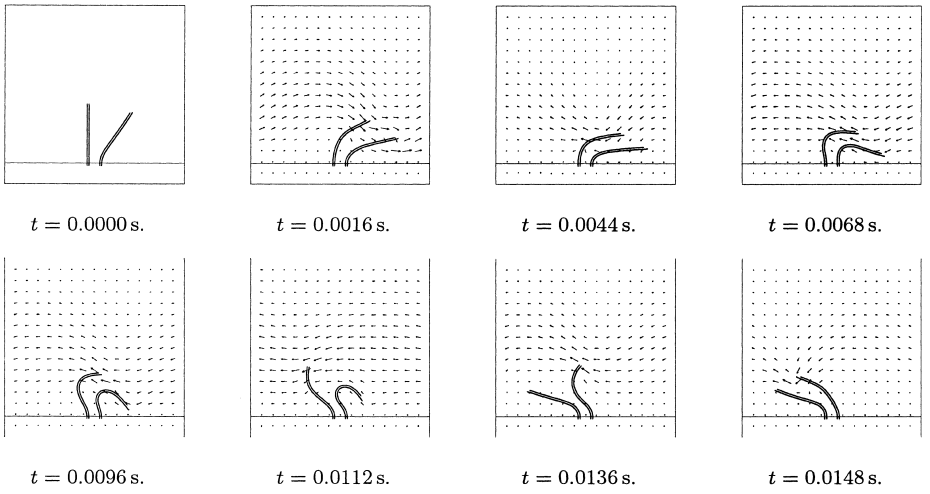

Figure 6. Synchronization of two cilia: at times $t = 0\,\mathrm{s}$ to $t = 0.0148\,\mathrm{s}$.

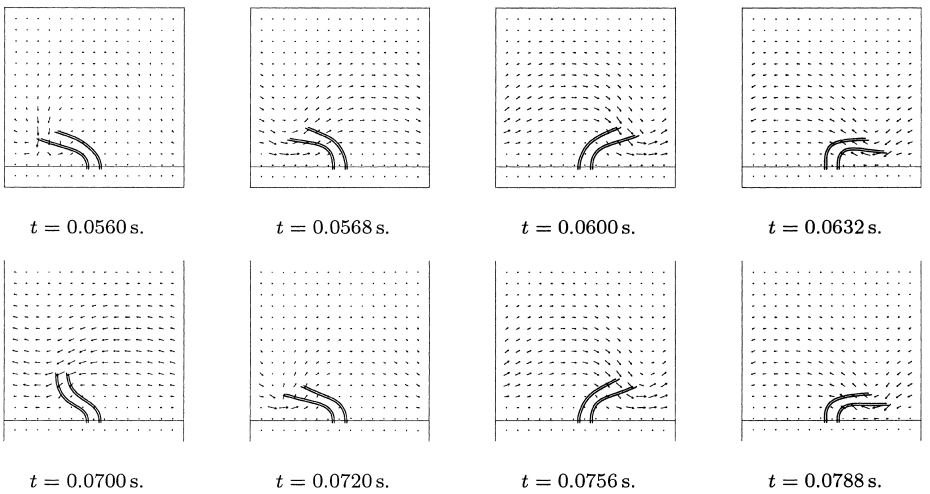

Figure 7. Synchronization of two cilia: at times $t = 0.0560\,\mathrm{s}$ to $t = 0.0888\,\mathrm{s}$.

more synchronization and have a beating frequency of about 59 Hz, which is the same as that in Figure 5. Simulations results (not shown) suggest that multiciliary interaction is subject to the spacing between cilia, fluid viscosity, and the switching algorithm.

5. DISCUSSION

Although the flagellar wave forms in the LAG and THRESHOLD models are very similar in some parameter ranges, the two models exhibit different responses to changes in fluid viscosity. There is experimental evidence that suggests a decrease in flagellar wavelength as a response to increasing fluid viscosity [28–31]. Thus, the preliminary simulation results shown here indicate that the THRESHOLD model is superior to the LAG model in its response to changes in fluid viscosity. We are currently conducting a detailed study of this issue.

A critical issue in multiciliary interaction is the mechanism for switching between effective and recovery modes. In the geometric switch model used here, the cilia switch directions once the bend angle exceeds a critical threshold, or equivalently, there is sufficient shear at the ciliary tips. This mechanism works well with one or two cilia but may break down when more cilia are introduced into the system. In this case, the reversal of one cilium can impede the motion of

neighboring cilia. We are developing an alternative model for the switching mechanism which includes shear velocity as well as shear. In addition, we are developing three-dimensional versions of these models.

REFERENCES

1. G.I. Taylor, Analysis of the swimming of microorganisms, *Proc. R. Soc. Lond.*, 447–61, (1951).
2. J. Gray and G. Hancock, The propulsion of sea-urchin spermatozoa, *J. Exp. Biol.* **32**, 802–814, (1955).
3. J.L. Lighthill, Flagellar hydrodynamics, *SIAM Review* **18**, 161–230, (1976).
4. L.J. Fauci and R. Dillon, Biofluidmechanics of reproduction, *Ann. Rev. Fluid Mech.* **38**, 371–94, (2006).
5. M. Murase, *The Dynamics of Cellular Motility*, John Wiley, Chichester, (1992).
6. G.B. Witman, Introduction to cilia and flagella, In *Ciliary and Flagellar Membranes*, (Edited by R.A. Bloodgood), pp. 1–30, Plenum, New York, (1990).
7. R. Dillon and L.J. Fauci, An integrative model of internal axoneme mechanics and external fluid dynamics in ciliary beating, *J. Theor. Biol.* **207**, 415–430, (2000).
8. C.S. Peskin, Numerical analysis of blood flow in the heart, *J. Comp. Phys.* **25**, 220–252, (1977).
9. R. Dillon, L.J. Fauci and C. Omoto, Mathematical modeling of axoneme mechanics and fluid dynamics in ciliary and sperm motility, *Dynamics of Continuous, Discrete and Impulsive Systems: Series A* **10**, 745–757, (2003).
10. C.S. Peskin, The immersed boundary method, *Acta Numerica*, 1–39, (2002).
11. R. Mittal and G. Iaccarino, Immersed boundary methods, *Ann. Rev. Fluid Mech.* **37**, 239–261, (2005).
12. L.J. Fauci and A. McDonald, Sperm motility in the presence of boundaries, *Bull. Math. Biol.* **57** (5), 679–699, (1995).
13. A.L. Fogelson, A mathematical model and numerical method for studying platelet adhesion and aggregation during blood clotting, *J. Comp. Phys.* **56**, 111–134, (1984).
14. R. Dillon, L.J. Fauci, A. Fogelson and D.P. Gaver, Modeling biofilm processes using the immersed boundary method, *J. Comp. Phys.* **129**, 57–73, (1996).
15. R. Dillon and L. Fauci, A microscale model of bacterial and biofilm dynamics in porous media, *Biotechnol. Bioeng.* **68**, 536–547, (2000).
16. C.S. Peskin and D.M. McQueen, A three-dimensional computational model for blood flow in the heart i. Immersed elastic fibers in a viscous incompressible fluid, *J. Comp. Phys.* **81**, 372–405, (1989).
17. C.S. Peskin and D.M. McQueen, A three-dimensional computational model for blood flow in the heart ii, *J. Comp. Phys.* **82**, 289–297, (1989).
18. K.M. Arthurs, L.C. Moore, C.S. Peskin, E.B. Pitman and H.E. Layton, Modeling arteriolar flow and mass transport using the immersed boundary method, *J. Comp. Phys.* **147**, 402–440, (1998).
19. R. Dillon and H.G. Othmer, A mathematical model for outgrowth and spatial patterning of the vertebrate limb bud, *J. Theor. Biol.* **197**, 295–330, (1999).
20. C.D. Eggleton and A.S. Popel, Large deformation of red blood cell ghosts in a simple shear flow, *Phys. Fluids* **10**, 1834–1845, (1998).
21. D.C. Bottino, Modeling viscoelastic networks and cell deformation in the context of the immersed boundary method, *J. Comp. Phys.* **147**, 86–113, (1998).
22. C.J. Brokaw, Computer simulation of flagellar movement. I. Demonstration of stable bend propagation and bend initiation by the sliding filament model, *Biophys. J.* **12**, 564–586, (1972).
23. C.J. Brokaw and D.R. Rintala, Computer simulation of flagellar movement III. Models incorporating cross-bridge kinetics, *J. Mechanochem. Cell Motil.* **3**, 77–86, (1975).
24. M. Hines and J.J. Blum, Bend propagation in flagella. I. Derivation of equations of motion and their simulation, *Biophys. J.* **23**, 41–57, (1978).
25. M. Hines and J.J. Blum, Bend propagation in flagella. II. Incorporating of dynein cross-bridge kinetics into the equations of motion, *Biophys. J.* **25**, 421–442, (1979).
26. C.J. Brokaw, Computer simulation of flagellar movement VIII: Coordination of dynein by local curvature control can generate helical bending waves, *Cell Motil. Cytoskeleton* **53**, 103–124, (2002).
27. C.J. Brokaw, Computer simulation of flagellar movement IX: Oscillation and symmetry breaking in a model for short flagella and nodal cilia, *Cell Motil Cytoskeleton* **60**, 35–47, (2005).
28. C.J. Brokaw, Effects of viscosity and ATP concentration on the movement of reactivated sea-urchin sperm flagella, *J. Exp. Biol.* **62**, 701–719, (1975).
29. C.J. Brokaw, Microtubule sliding, bend initiation, and bend propagation parameters of *ciona* sperm flagella altered by viscous load, *Cell. Motil. Cytoskeleton* **33**, 6–21, (1996).
30. C.J. Brokaw, Simulating the effects of fluid viscosity on the behavior of sperm flagella, *Math. Meth. Appl. Sci.* **24**, 1351–1365, (2001).
31. G.I. Taylor, Reactivation of sea-urchin sperm flagella induced by rapid photolysis of caged ATP, *J. Exp. Biol.* **201**, 1493–1503, (1998).